Magnetohydrodynamic Simulations of the Geodynamo

Helmut Harder, Stephan Stellmach, Ulrich Hansen

Magnetohydrodynamic Simulations of the Geodynamo

Helmut Harder, Stephan Stellmach, and Ulrich Hansen

Institute of Geophysics
University Münster, 48148 Münster, Germany
E-mail: {harder,stellma,hansen}@earth.uni-muenster.de

The generation of the interior magnetic field of the Earth is studied by numerical simulations of the magnetohydrodynamic dynamo problem. The main problem is to reach extreme parameter values relevant to the Earth's molten, electrically conductive iron core. With simplified cartesian models we are able to perform calculations in the relevant regime where viscous forces are small compared to rotational Coriolis and magnetic Lorentz forces. As theoretically predicted, these simulations show that the generated magnetic field tends to break the Taylor Proudman theorem and that it promotes a vigorous, large-scaled flow in the fluid core. For the more Earth-like case of dynamo action within a spherical shell, a new parallel finite volume approach is in progress. A comparison with published benchmark solutions shows the accuracy, but also the limitations, of this method.

1   Introduction

Seismological studies of the propagation of elastic waves have shown that the Earth's outer core, in a depth of about 3000 to 5000 km, consists of molten iron. Slight density variations in this liquid, electrically conductive layer drive a convective flow, which inturn generates and maintains the magnetic field of the Earth. Density variation in the fluid outer core are induced by the secular cooling of the Earth and by the freezing of the inner, solid core. Due to the importance of the magnetic field and its occasional reversals to terrestrial life, a proper understanding of the dynamo processes in the core is one of the grand challenges in modern geophysics.

Numerical simulations of the dynamo processes are extremely time intensive and have only become feasable during the past decade by the increased power of modern computer architectures. Still up to now, numerical simulations are possible only in a parameter regime far from values expected for the Earth's core. Especially the low values of viscosity and of thermal and compositional diffusivities pose severe difficulties which have not been overcome yet.

In this study, we use the plane layer dynamo model originally proposed by Childress and Soward[1–3] to investigate the regime of low viscosity. A very useful parameter to indicate the strength of viscous effects is the Ekman number $E = \nu/2\Omega L^2$ which is defined as the ratio of the rotational time scale to the time scale of viscous dissipation. Typically, spherical models are able to reach $E = O(10^{-4})$ if all diffusion operators are retained in the classical form. The geometrical simplicity of our cartesian model allows us to preform calculations at $E = 5 \times 10^{-6}$. This low value allows us to investigate effects which are absent in the high Ekman number regime and which are thus very difficult to study in spherical geometry.

Nevertheless, we think that also in the case of spherical models progress could be made in this respect. Based on the experience gained by the cartesian models, we have currently developed a finite volume method to solve the spherical dynamo problem. Since

this approach is much more suitable for parallel computation than a spectral transform method, which up to now is dominantly used in spherical dynamo simulations, we hope that a much higher grid resolution could be used in future simulations. This will allow to shift parameter values towards a more Earth-like regime. However, extensive tests of the new method are needed, before such computatial demanding simulations could be started. A comparison with benchmark results obtained previously by spectral methods demonstrates the prospects of the finite volume approach.

2   Mathematical Model

The model consists of an incompressible electrically conducting fluid layer confined between planes which is heated from below and rotates with angular velocity $\mathbf{\Omega}$ about a vertical axis $\mathbf{e_z}$. Under these conditions the equations governing magnetohydrodynamic dynamos are the coupled heat transport equation, Navier Stokes equations with Coriolis and Lorentz terms included, the magnetic induction equation, and constraints to ensure solenoidal vector fields $\mathbf{u}$ and $\mathbf{B}$, i.e.

$$\frac{\partial \mathbf{u}}{\partial t} + \nabla.\Big(\mathbf{u}\mathbf{u} - \frac{Pr}{Rb}\mathbf{B}\mathbf{B}\Big) - P_r\nabla^2\mathbf{u} + \nabla P + \frac{Pr}{E_k}\mathbf{e}_z \times \mathbf{u} - P_r R_a T\mathbf{a} = 0, \quad (1)$$

$$\frac{\partial \mathbf{B}}{\partial t} + \nabla.\Big(\mathbf{u}\mathbf{B} - \mathbf{B}\mathbf{u}\Big) - \frac{1}{Rb}\nabla^2\mathbf{B} = 0, \quad (2)$$

$$\frac{\partial T}{\partial t} + \nabla.\Big(\mathbf{u}T\Big) - \nabla^2 T = 0, \quad (3)$$

$$\nabla\mathbf{u} = \nabla\mathbf{B} = 0, \quad (4)$$

where P denotes the pressure, $\mathbf{u}$ the vector of fluid flow, $\mathbf{B}$ the vector of magnetic induction, T the temperature, and $\mathbf{e_z}$ the unit vector parallel to the axis of rotation. In the cartesian case $\mathbf{a} = \mathbf{e_z}$ holds, whereas in the spherical case $\mathbf{a} = \mathbf{r}/r_0$ is valid, where r_0 denotes the radius to the outer boundary. By the scaling of the equations the following four dimensionless numbers are intoduced:

Rayleigh number $Ra = \alpha\Delta T g d^3/(\kappa\nu)$,   Ekman number $E = \nu/(2\Omega d^2)$

Prandtl number $Pr = \nu/\kappa$,   Roberts number $Rb = \kappa/\eta$.

The Rayleigh number Ra defines the ratio of buoyancy forces to viscous forces, the Ekman number E is the ratio of viscous forces to the Coriolis force, whereas Prandtl Pr and Roberts numbers Rb are ratios of diffusivities. In these definitions α denotes the coefficient of thermal expansion, κ the thermal diffusivity, ν the dynamical viscosity, η magnetic viscosity, g_0 gravity at the outer boundary, Ω the rotation rate, ΔT the temperature difference, and d the distance of outer to inner boundary.

In the cartesian case we apply isothermal, free slip and electrically perfect conducting top and bottom boundaries. Horizontal boundaries are periodic. In the spherical case isothermal, rigid and quasi vacuum[4] ($\mathbf{r} \times \mathbf{B} = 0$) conditions are applied. The applied magnetic boundary conditions are not realistic and are chosen for numerical convenience only.

3 Numerical Method

In the cartesian method we solve the magnetohydrodynamic equations (1-4) with a primitive variable approach. The spatial discretization is done by a cell centered (collocated) finite volume method, where the diffusive term are calculated by a central approximation, whereas advection term are approximated by an upwind-biased QUICK scheme. Time stepping is performed by a second order BDF scheme.

The computational grid is divided by domain decomposition and each domain is attributated to a processor. We use the Message Passing Interface (MPI) to communicate values at domain boundaries to neighboring processes. The domains overlap by two grid cells to include values of neighboring domains. The overlap of two cells follows from the approximation of advection terms by the QUICK scheme.

We use a block Gauss Seidel iteration to calculate temperature, magnetic induction and velocity in a fully implicit fashion. Since only small timesteps are used, usually very few SIMPLE iterations suffice to reduce the residuals by 5 orders of magnitude. To calculate the pressure and magnetic field correction, which is the most compute intensive part of the algorithm, we use the Krylov subspace method BiCGSTAB. A more detailed description of the fully implicit method is available[5].
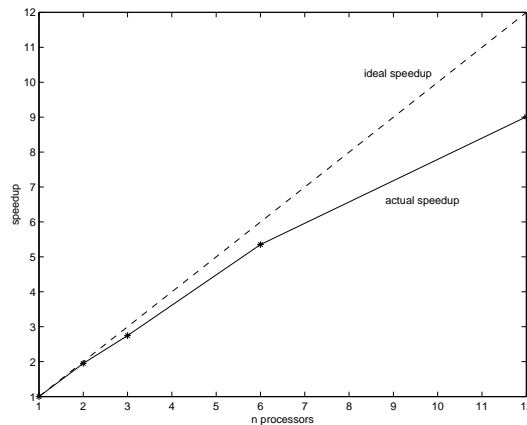

Figure 1. Speedup of the spherical calculation by the use of n processes.

The spherical method has some similiarities with our cartesian approach. The finite volume discretization is in this case generated by the projection of an equidistant mesh of the enscribed cube onto the unit sphere, followed by an orthogonalization of the grid. In the 3. spatial dimension we use an non-equidistant discretisation of the radius. By this method, we project topologically a spherical shell to six coupled cubes, which is convenient for parallel computation.

The most important deviation from the cartesian method is the different implementation of the collocated grid arrangment. Here we use pressure weigthed interpolation (PWI)[6] to calculate normal components at the cell surfaces which are needed to fullfill the incompressibiliy condition. This method has been successfully tested for several sim-

ple convection problems. The scalability of the code is demonstrated in Figure 1. The calculations were performed at our local Pentium cluster on a grid with 6×32^3 cells.

4 Dynamo Calculations

4.1 Cartesian Geometry

To get a proper understanding of the dynamo processes at low Ekman number, our approach is to chose the Ekman number as low as possible while adjusting the other parameters in a way that keeps the numerical cost at a minimum. The parameters for the run presented here are $a = b = 1, E = 5 \times 10^{-6}, Pr = 1, Rb = 1$ and $Ra = 1.2 \times 10^8$. The spatial resolution is 128^3 control volumes. The dynamo is initiated by inserting a small magnetic field into fully developed non-magnetic convection. Figure 2 shows the
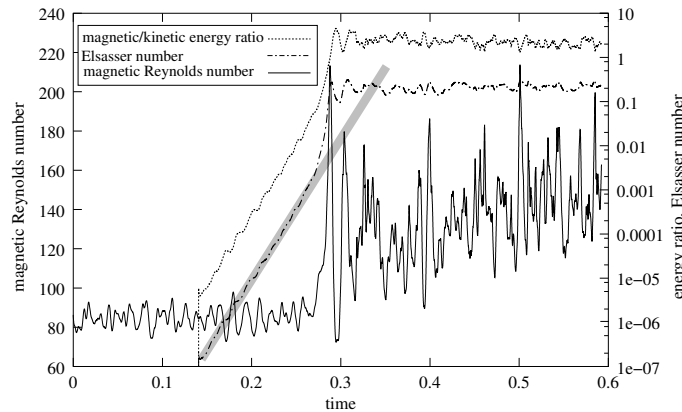

Figure 2. Temporal evolution of the magnetic Reynolds number Re_m, which is proportional to the mean flow velocity, the Elsasser number Λ, which is proportional to the mean magnetic energy, and the dimensional ratio of magnetic to kinetic energy for $E = 5 \times 10^{-6}, Ra = 1.2 \times 10^8, Pr = Rb = 1$. The grey bar indicates the phase of kinematic growth characterized by a constant mean growth rate.

temporal evolution of the magnetic Reynolds number $Re_m := < Rb \sqrt{\mathbf{u}^2} >_\mathcal{V}$, the Elsasser number $\Lambda := < E \mathbf{B}^2 >_\mathcal{V}$ and the ratio of dimensional magnetic to kinetic energy $E_{mag}/E_{kin} := (Rb\ Pr/E)\Lambda/Re_m$ where $< ... >_\mathcal{V}$ denotes a volume average over the computational domain $\mathcal{V}$. We firstly calculated a non-magnetic solution and inserted a small magnetic perturbation after a statistically stationary state was reached. This perturbation is amplified by the convective flow through kinematic dynamo action until the magnetic field becomes strong enough to significantly influence the flow pattern. As the magnetic field grows, the magnetic Reynolds number and correspondingly the convective velocities of the flow increase. Figure 2 shows that this again leads to more efficient dynamo action resulting in very fast, non-exponential growth of the field strength until saturation occurs. This strongly indicates a tendency of the magnetic field to promote convection.
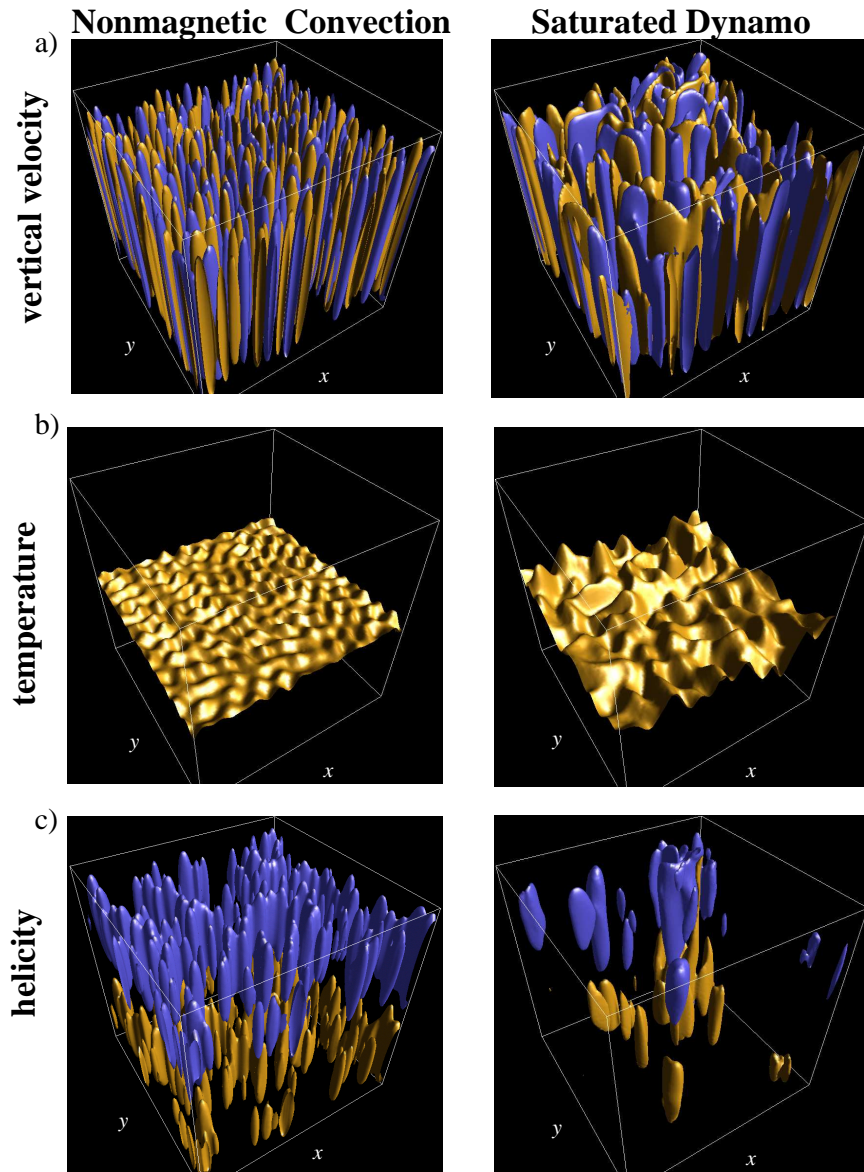
Figure 3. Comparison of typical flow structures for non-magnetic convection (left column) and the corresponding magnetically saturated dynamo solution (right column) for $E = 5E-6$, $Pr = 1$, $Rb = 1$ and $Ra = 1.2 \times 10^8$. The upper row *a)* shows isosurfaces at $u_z = 50$ (yellow) and $u_z = -50$ (blue). *b)* shows an iso-surface of temperature at $T = 0.5$. The lowermost plot *c)* shows iso-surfaces of helicity $H = \mathbf{u} \cdot (\nabla \times \mathbf{u})$ at $\pm 20\%$ of the maximum value. Here, blue indicates negative and yellow indicates positive helicity.

To give an impression of the resulting flow structures, we present visualizations in figure 3. The pictures on the left side show the non-magnetic solution while the corresponding
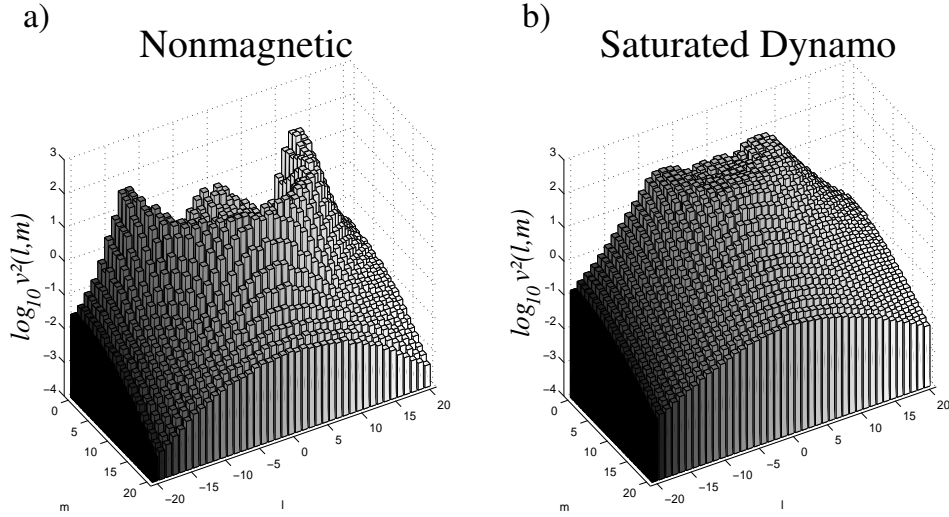
Figure 4. Time averaged spectral distribution of kinetic energy for *a)* the nonmagnetic and *b)* the dynamo case. The time average was taken over a time interval covering the nonmagnetic and the saturated period.

saturated dynamo solution is displayed on the right. The top row *a)* shows isosurfaces of u_z at $u_z = \pm 50$. The next row *b)* shows an iso-surface of the temperature field at $T = 0.5$. In the dynamo case, the iso-surface is much more deformed than in the non-magnetic case illustrating the convection promoting character of the magnetic field. The last row *c)* shows iso-surfaces of helicity $H = \mathbf{u} \cdot (\nabla \times \mathbf{u})$ at $\pm 20\%$ of its maximum absolute value. For both the non-magnetic and the dynamo case, the velocity field consists of vertical columns with positive helicity in the lower and negative helicity in the upper half of the layer. These columns move through the domain in an irregular fashion. By comparing the non-magnetic and the dynamo solution, it can be anticipated from figure 3 that the relevant spatial scales increase through the action of the magnetic field.

To quantify this effect we calculate the spectra

$$\mathbf{u} = \sum_{l,m,n} \mathbf{u}_{l,m,n} \exp(2\pi i(lx + my))(cos(n\pi z), cos(n\pi z), sin(n\pi z)) \qquad (1)$$

of the solution. The plots shown in figure 4 show the l, m-distribution of the quantity $\log_{10} v^2(l,m) = \log_{10} < \sum_{n} E(l,m,n) >$, where $E(l,m,n)$ denotes the dimension-less kinetic energy in the mode with wavenumbers l, m and n. Here $< .. >$ indicates a time average. Only horizontal wavenumbers up to 20 have been plotted to highlight differences between the dynamo and the non-magnetic solution. For the non-magnetic case, the most striking features are very pronounced maxima for modes of wavenumbers $11 \leq k := \sqrt{l^2 + m^2} \leq 14$ while modes with both lower and higher k contain by far less energy. A second local maximum exists for long wavelength modes, but its contribution to the entire kinetic energy is small.

The kinetic energy spectrum for the dynamo case is considerably different. As compared to the non-magnetic case, the spatial scales increase, the sharp peaks at higher

394

wavenumbers nearly disappear and the energy spectrum rapidly drops off for modes with $k \geq 9$. The whole time averaged kinetic energy exceeds the corresponding non-magnetic value by roughly a factor of 2.5.
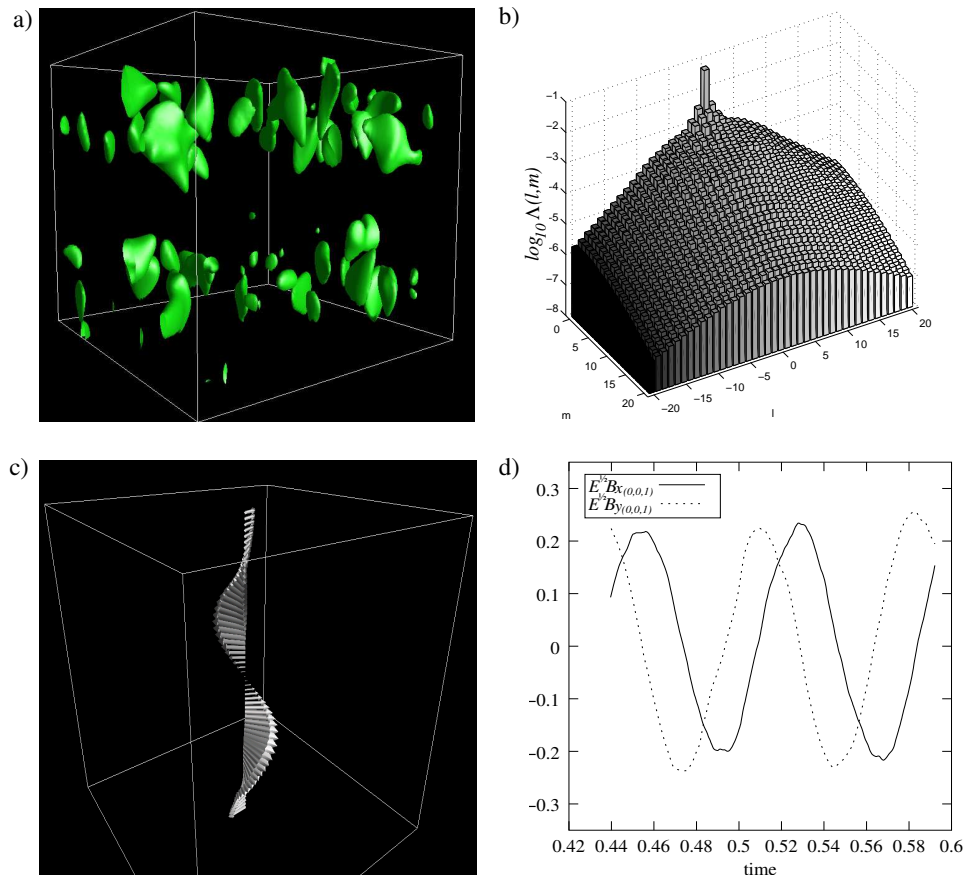

Figure 5. Visualization of the structure of the generated magnetic field. The upper picture on the left side *a)* shows an iso-surface of the magnetic energy at 20% of its maximum value. Plot *b)* shows the spectral distribution of the magnetic energy based on the Elsasser number among the horizontal modes (see text for details). The left picture in the bottom row *c)* is a plot of the horizontally averaged magnetic field. Again, the arrows are scaled by the absolute value. Plot *d)* shows the time history of the Fourier coefficients $B_{x_{(0,0,1)}}$ and $B_{y_{(0,0,1)}}$.

The structure of the magnetic field is shown in figure 5. The left picture shows a snapshot of an iso-surface of the magnetic energy density at 20% of its maximum value at the displayed time step. The time averaged spectral distribution of magnetic energy is shown in the second image in the upper row. The magnetic field is expanded in Fourier series as above in the case of the velocity field. Most of the magnetic energy is contained in modes with $(l, m) = (0, 0)$ corresponding to the so called mean field $\mathbf{B}_\perp := \overline{(B_x, B_y, 0)}$ where the bar indicates a horizontal average. Small scale convection feeds energy into the high

wavenumber components of the magnetic field which then moves up the spectrum in an inverse cascade. In sharp contrast to the velocity field, the magnetic spectrum monotonically decreases with increasing k.

Since the magnetic field is strongly dominated by modes with $k = 0$, which play a key role in the dynamo process, we give a visualization of the mean field in figure 5, where again arrows are scaled by its absolute value. The mean field is nearly antisymmetric with respect to the plane $z = 0.5$ which can be interpreted as a consequence of the fact that under the chosen magnetic boundary condition, the z-integrated mean field has to vanish[7]. $\mathbf{B}_\perp$ resembles a spiral staircase twisting in the same sense as the velocity field. Together with the helicity, at $z = 1/2$ the sense of twisting of the mean field changes sign. The appearance of this spiral staircase structure of $\mathbf{B}_\perp$ is best understood by picturing each half of the layer as a crude representation of a G.O. Roberts dynamo[8].

The time evolution of the mean field is quite simple. To illustrate this, the last picture of figure 5 shows the temporal evolution of the $(0, 0, 1)$-mode of the horizontal magnetic field. The plot is typical for the strongest mean-field modes which are primarily the odd modes. The mean field rotates in a sense opposite to $\mathbf{\Omega}$ with a period of the order of the free decay time of the system.

4.2 Spherical Geometry

In spherical geometry we test the finite volume approach in the case of non-magnetic convection within a rotating spherical shell. The benchmark case[9] is defined by Rayleigh number $Ra = 10^5$, Prandtl number $Pr = 1$, Ekman number $E = 5 \times 10^{-4}$, and ratio of the radii to lower and outer boundary $r_l/r_0 = 7/13$. The solution is quasi-stationary and is characterized by four uprising and four descending Busse-Taylor columns. After a transient period of about one thermal diffusion time, the time-dependency of the solution is reduced to a slow azimuthal drift. However, since the grid is not rotationally invariant, slight variations are introduced, which depend on the momentary azimuthal position of the solution on the grid. The solution is identical after an azimuthal drift of 90 degrees, which is the common periodicity of both the grid and the solution. A convergence test of the average flow velocity v_{rms} and a local velocity v_ϕ, defined at a specified feature of the solution, demonstrates that these variations are reduced with the square of the grid resolution (Figure 6), as it is expected with a second order convergent method. A Romberg extrapolation of the results is in excellent agreement with the best estimates obtained by various spectral and semi-spectral transform methods[9].

The full dynamo problem has been solved in a series of simulations with Roberts numbers ($Rb = 8, 5, 4, 1$), all other parameter as before. In accordance with the benchmark results, stable dynamos are obtained only for $Rb > 4$, for smaller Rb the initial magnetic field decays exponentially. Figure 7 displays the time evolution of the spatially averaged magnetic induction ($Rb = 8$). After approximately one magnetic diffusion time ($t = 8$) a quasi-stationary magnetic field is obtained. The flow structure is similiar to the case of non-magnetic convection, which indicates that Lorentz forces are of minor importance in this model. The magnetic field is strongly concentrated within flux bundles in the descending Busse Taylor columns (Figure 7). Due to different magnetic boundary conditions a more quantitative comparison to benchmark results is not feasible in this case.
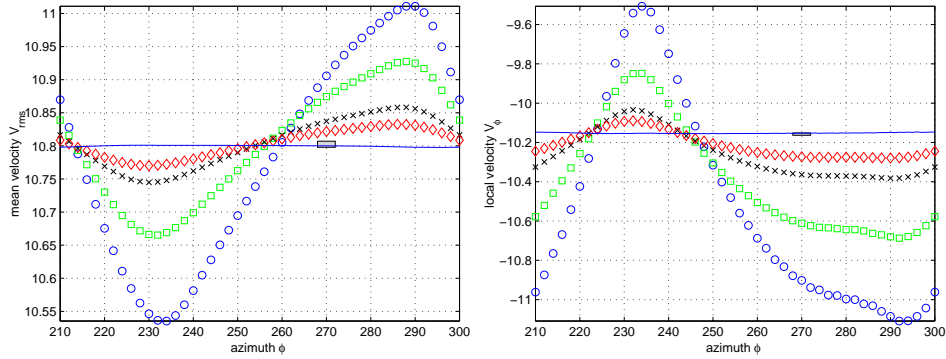
Figure 6. Root mean square velocity v_{rms} and local azimuthal velocity v_ϕ for different resolution and azimuthal grid position ϕ. Grid resolution is $6 \times n^3$, circles $n = 24$, squares $n = 32$, crosses $n = 48$, diamonds $n = 64$, and solid line indicates the Romberg extrapolation of the results. Shaded rectangle at $\phi = 270$ gives the benchmark solution with uncertainties[9].
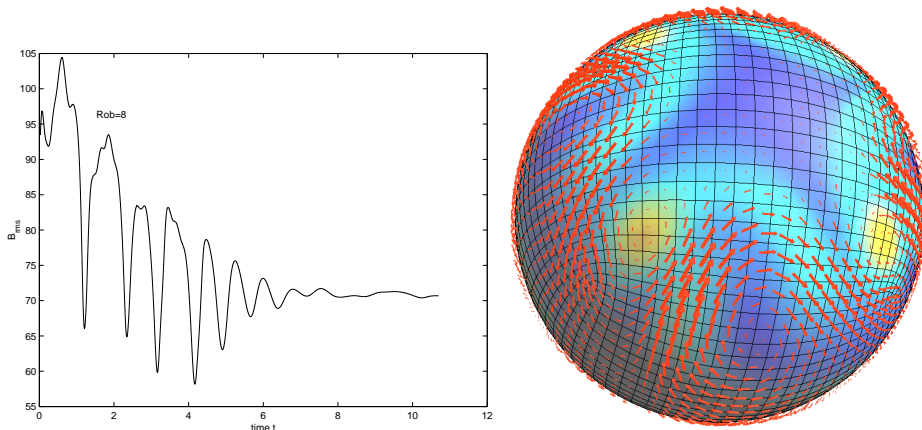

Figure 7. Time evolution of the spatially averaged magnetic induction (left). Amplitude of magnetic induction $|\mathbf{B}|$ (colour coded: red high intensity and blue low intensity) and flow velocity (arrows) below the top Ekman boundary layer (right). It should be noted that the indicated spherical grid is not rotationally invariant.

5 Discussion

By comparing cartesian nonmagnetic and magnetic solutions, we find that the magnetic field strongly promotes convection in the low Ekman number regime consistently with results from magnetoconvection theory[10, 11]. As would be expected, the magnetic field acts to weaken the rotational constraint leading to a decrease in the size of the convection cells as compared to the nonmagnetic solution. We are thus in a parameter regime where the flow field is substantially altered by the action of the Lorentz force.

The spherical simulations are obtained in the moderate Ekman number regime. However, the results are encouraging, especially the comparison to benchmark solutions. We

anticipate that in the near future simulations in a more Earth-like regime are possible. However, such simulations will be computationally expensive and certainly require parallel high performance architectures.

Acknowledgments

References

1. S. Childress and A.M. Soward. Convection-driven hydromagnetic dynamo. *Phys. Rev. Lett.*, 29:837–839, 1972.
2. A.M. Soward. A convection driven dynamo I: The weak field case. *Phil. Trans. R. Soc. Lond. A*, 275:611–651, 1974.
3. Y. Fautrelle and S. Childress. Convective dynamos with intermediate and strong fields. *Geophys. Astrophys. Fluid Dynamics*, 22:235–279, 1982.
4. A. Kageyama and T. Sato. Generation mechanism of a dipole field by a magnetohydrodynamic dynamo. *Phys. Rev. E*, 55:4617–4626, 1997.
5. J. Schmalzl and U. Hansen. A fully implicit model for simulating dynamo action in a cartesian domain. *Phys. Earth planet. Inter.*, 120:339–349, 2000.
6. T.F. Miller and Schmidt F.W. Use of a pressure-weighted interpolation method for the solution of the incompressible navier-stokes equations on a nonstaggered grid system. *Numer. Heat Transfer*, 14:213–233, 1988.
7. C.A. Jones and P.H. Roberts. Convection driven dynamos in a rotating plane layer. *J. Fluid Mech.*, 404:311–343, 2000.
8. G.O. Roberts. Dynamo action of fluid motions with two-dimensional periodicity. *Phil. Trans. R. Soc. Lond.*, A271:411–454, 1972.
9. U. Christensen and 15 coauthors. A numerical dynamo benchmark. *Phys. Earth planet. Inter.*, 128:25–34, 2001.
10. P.H. Roberts and C.A. Jones. The onset of magnetoconvection at large Prandtl number in a rotating layer I. Finite magnetic diffusion. *Geophys. Astrophys. Fluid Dynamics*, 92:289–325, 2000.
11. I.A. Eltayeb. Hydromagnetic convection in a rapidly rotating fluid layer. *Proc. R. Soc. Lond. A.*, 326:229–254, 1972.